RSC Advances

PAPER

View Article Online
View Journal | View Issue



Cite this: *RSC Adv.*, 2022, **12**, 22465

# Photocatalytic activity of layered $MoS_2$ in the reductive degradation of bromophenol blue†

Joanna Kisała, *[a] Ana M. Ferraria, [bc] Nataliya Mitina,[d] Bogumił Cieniek, [e] Piotr Krzemiński, [f] Dariusz Pogocki, [g] Roman Nebesnyi,[h] Oleksandr Zaichenko[d] and Yaroslav Bobitski[fi]

Received 30th May 2022
Accepted 28th July 2022

DOI: 10.1039/d2ra03362c

rsc.li/rsc-advances

Molybdenum disulphide ($MoS_2$) is a layered material with interesting photocatalytic properties. In this study, a layered $MoS_2$ was produced using a hydrothermal method. The obtained material was characterised by XRD (X-ray diffraction), XPS (X-ray photoelectron spectroscopy), SEM (scanning electron microscopy), UV-Vis spectroscopy, DLS (dynamic light scattering), and zeta potential analysis. For the evaluation of the photocatalytic properties of layered $MoS_2$, a solution of bromophenol blue (BPB) and the catalyst was illuminated for 120 minutes. According to the experimental results, $MoS_2$ exhibited excellent catalytic activity in BPB degradation. The $MoS_2$ preparation method enabled improved light harvesting, avoided fast charge recombination (related to bulk $MoS_2$), and created a large number of suitable electron transfer sites for photocatalytic reactions. Simulation of BPB decay and bromide production was carried out for a further understanding of $MoS_2$ photocatalytic action. The simulation results proved the reduction mechanism of BPB photodegradation.



## 1. Introduction

In 2019, the WHO (World Health Organisation) declared that over 2.2 billion humans do not have access to clean water. Continuous shrinking reserves of global drinking water are caused in part by water pollution. Water contamination, causing serious environmental and health problems, has gained a lot of attention worldwide. The low-cost wastewater decontamination would be a partial remedy for the emerging crisis. A meeting of the demands of environmental remediation is a great challenge for society, especially for scientists, researchers, and process engineers.

The wastewater from the textile industry, even with very low dye concentrations, can intensely colour the wastewater. Apart from negative visual effects, such aromatic compounds are highly non-biodegradable and mostly carcinogenic and mutagenic.[1] Usage of renewable energy sources, *i.e.*, solar energy, in the photocatalytic process is one of the efficient methods allowing the degradation of environmental pollutants caused by the industry.

Bromophenol blue (BPB) is an acid dye applied as a colour marker to monitor the process of agarose gel electrophoresis, polyacrylamide gel electrophoresis, for colouring proteins in paper electrophoresis, and as a pH indicator. This dye is widely used as an industrial dye for foods, drugs, cosmetics, textiles, printing inks, and as a laboratory indicator.[2] Additionally, BPB is a convenient model compound for the investigation of the photodegradation of structurally similar polyhalogenated bisphenols extensively used as flame retardants.[3–5]

Molybdenum disulphide ($MoS_2$), used here as a photocatalyst, is a semiconducting material with a layered structure, belonging to the family of transition metal dichalcogenides.[6–8] Solid molybdenum disulphide ($MoS_2$, molybdenite) is a chemically stable layered material, made up of two layers of sulphur atoms and a layer of molybdenum atoms, forming a sandwich-like structure.[9] Due to its peculiarity, it is widely used in the photoelectric conversion and as a photocatalyst.[10] Actually, it is a small-particle semiconductor with a small band gap, allowing valence-band electrons to be excited to the conduction band by

[a]*Department of Biology, Institute of Biology and Biotechnology, University of Rzeszow, Pigonia 1, 35-310 Rzeszow, Poland. E-mail: jkisala@ur.edu.pl*
[b]*BSIRG-iBB-Institute for Bioengineering and Biosciences, Universidade de Lisboa, 1049-001 Lisbon, Portugal*
[c]*Associate Laboratory i4HB—Institute for Health and Bioeconomy at Instituto Superior Técnico, Universidade de Lisboa, 1049-001 Lisboa, Portugal*
[d]*Department of Organic Chemistry, Institute of Chemistry and Chemical Technologies, Lviv Polytechnic National University, 79013 Lviv, Ukraine*
[e]*Institute of Materials Science, College of Natural Sciences, University of Rzeszow, Pigonia 1, 35-959 Rzeszow, Poland*
[f]*Centre for Microelectronics and Nanotechnology, Institute of Physics, University of Rzeszow, Pigonia 1, 35-959 Rzeszow, Poland*
[g]*Institute of Nuclear Chemistry and Technology, Dorodna 16, 03-195, Warsaw, Poland*
[h]*Technology of Organic Products Department, Lviv Polytechnic National University, 12S. Bandera St., Lviv, 79013, Ukraine*
[i]*Department of Photonics, Lviv Polytechnic National University, 1 Sviatoho Yura Sq., 79013 Lviv, Ukraine*

† Electronic supplementary information (ESI) available. See https://doi.org/10.1039/d2ra03362c

almost the entire range of the visible light spectrum. Additionally, the single-layer $MoS_2$ possesses excellent charge carrier mobility, as good as the carbon nanotube. The sheet structure has a superior surface-to-volume ratio that could be an advantage for catalysing materials.

Advanced oxidation processes (AOPs) have received a lot of attention in the literature in recent years. However, not all compounds can be effectively oxidised because, in fact, they already are in an oxidised form. This applies, for example, to organic compounds containing halogens.[11,12] Therefore, the need for an alternative to *in situ* oxidation processes has been recognised. Advanced reduction processes (ARPs) rely on the production of strongly reducing hydrated electrons ($e_{aq}^-$), which exhibit fast reaction rate constants with inorganic and organic compounds.

There is very little research available on the application of ARPs in the degradation of organic water pollutants. Current research is one of the few on this topic. In this paper, the authors present the synthesis of $MoS_2$ multilayer nanostructures by the hydrothermal method. Their morphology and structure were characterised by scanning electron microscopy (SEM), X-ray diffraction spectroscopy (XRD), atomic force microscopy (AFM), and Raman spectroscopy. The photocatalytic properties of $MoS_2$ in the degradation of bromophenol blue (BPB) as a model pollutant were assessed.

## 2. Experimental section

### 2.1 Materials

$Li_2MoO_4$ was used as the molybdenum source and $Na_2S$ was used as the sulphur source to prepare $MoS_2$. Lithium molybdate ($Li_2MoO_4$), sodium sulphide ($Na_2S$), and hydrazine dihydrochloride ($N_2H_4$ 2HCl) were purchased from Sigma-Aldrich (St Louis, MO, USA).

The hydrogen ion concentration of the investigated systems was adjusted by NaOH and HCl. Bromophenol blue (St Louis, MO, USA) was used as a representative dye to evaluate the photocatalytic properties of layered $MoS_2$. *Tert*-butanol was used in the experiment as the hydroxyl radical scavenger. All reagents were of analytical grade and were used as received.

### 2.2 Preparation of $MoS_2$

The synthesis of $MoS_2$ nanoparticles was carried out: at the first stage 5.4 g of $Li_2MoO_4$ was dissolved in 48.4 mL of 20% $Na_2S$ aqueous solution. After 30 minutes of constant stirring, $Li_2MoS_4$ precipitated under the reaction:

$$Li_2MoO_4 + 4Na_2S + 4H_2O \rightarrow Li_2MoS_4 + 8NaOH \quad (1)$$

Solid $Li_2MoS_4$ was mixed with a solution of hydrazine chloride (0.62 M $L^{-1}$) and the pH value of the reaction medium was adjusted to 7.8 by the addition of 0.1 M $L^{-1}$ HCl solution. Afterwards, the suspension was inserted into the Teflon coated autoclave and heated for 24 h at 473 K. The resulting precipitate of black colour was washed out with distilled water three times and finally with ethyl alcohol. The solid was separated by centrifugation and dried at 313 K.

### 2.3 Photocatalyst characterisation

The morphology and particle size of prepared nanoparticles were evaluated by a field emission scanning electron microscope (FESEM) Helios NanoLab 650 (FEI, Hillsboro, Oregon, USA) operating at 5 kV and 18 kV using ETD detector with Secondary Electron (SE) imaging mode. The $MoS_2$ nanoparticles were mounted on a specimen table using conductive carbon tape. Images were taken at different magnifications and measurements were conducted on visibly separated nanoparticles. The specimen was uncoated.

Atomic force microscopy (AFM) measurements were performed using a Solver Nano II Microscope (NT-MDT Spectrum Instruments LLC, Tempe, Arizona, USA). The solution of the $MoS_2$ was deposited on the substrate following the drop casting method. The samples were evaporated in desiccator during 24 hours. Evaporated sample was analysed using tapping mode.

XRD patterns were recorded with an X-ray diffractometer (D8 Advance, Bruker, Germany) and 0.15406 nm Cu $K_\alpha$ radiation. The average crystallite sizes ($D$) of $MoS_2$ samples were calculated from the powder XRD line widths by applying the Debye–Scherrer eqn (2)[13,14]

$$D = \frac{0.89\lambda}{B\cos\theta} \quad (2)$$

where $\lambda$ is the wavelength of the X-ray in nanometres, $B$ is the peak width at half-height (FWHM), and $\theta$ is the angle between the incident and diffracted beams in angular degrees.

The Raman spectra were obtained using an inVia Micro Raman Renishaw spectrometer combined with a Leica DM 2500 M microscope (Renishaw, Wotton-under-Edge, UK) equipped with a 633 nm laser as an excitation source. The measurements were taken with an exposure time of 10 s with triple scan accumulation and for the laser output power of 1.5 mW. The data were collected in the spectral range of 100–1500 $cm^{-1}$ with spectral resolution over 2 $cm^{-1}$. The measurement was carried out with a 50× lens magnification and choosing five random positions. Baseline correction was performed during data processing.

The powdered $MoS_2$ sample was analysed by X-ray photoelectron spectroscopy (XPS) with a dual anode non-monochromatic XSAM800 spectrometer from KRATOS (Kratos Analytical Ltd, Manchester, UK). Al $K_\alpha$ X-rays ($h\nu$ = 1486.6 eV) were used. The acquisition conditions were as published elsewhere.[15] The $MoS_2$ powder was fixed with a silicone-based double face tape, completely covering the XPS holder and analysed at TOA = 45°. No flood gun was used for charge neutralisation. The charge shift was corrected using as a reference the binding energy (BE) of $sp^2$ C–C and/or C–H, centred at 284.7 eV. Source satellites were subtracted. Pseudo-Voight profiles (Gaussian–Lorentzian (GL) products) were used for peak fitting with the XPSPeak4.1 software (freeware). Shirley baselines were used. The sensitivity factors used for the quantification analysis were those of the library of Vision 2 for Windows, Version 2.2.9 from KRATOS.

The optical measurements of the catalysts were carried out using an Agilent Technologies Cary Series UV-Vis-NIR

spectrophotometer (Agilent, Santa Clara, CA, USA) in the wavelength range of 180 to 1200 nm. The UV-Vis spectra of organic compounds solutions were measured on a VWR UV-VIS 3100 PC spectrophotometer (VWR International Ltd, Gdansk, Poland).

The hydrodynamic diameter of the semiconductor particles and the electrokinetic potential (zeta potential, $\zeta$ potential) were measured as a colloidal dispersion with a concentration of 1.25 $\times$ $10^{-1}$ g $L^{-1}$. The zeta potentials were determined by electrophoretic mobility measurement in a particle suspension. The hydrodynamic diameter of the catalysts was measured by Dynamic Light Scattering (DLS). These measurements were performed with the NanoPlus 3 HD analyser (Particulate Systems, Micromeritics, Norcross, GA 30093, USA).

### 2.4 Photocatalytic experiment conditions

The photocatalytic activity of the $MoS_2$ catalyst was evaluated by monitoring the degradation of bromophenol blue (BPB). 250 mL of 1.0 $\times$ $10^{-4}$ M $L^{-1}$ BPB solution, 0.05 g of catalyst powder, and 0.3 M $L^{-1}$ *t*-BuOH were placed in the photoreactor. The resulting suspension, pH 5.2, was then stirred for 30 minutes in the dark under argon. The photocatalytic degradation was performed using a Heraeus LRS2 photoreactor in a continuous argon flow. The illumination was effected with the excimer lamp TQ150 (150 Watt, with forced water cooling down to 25 °C, of 47 W light energy flux of power density 4.696 mW $cm^{-2}$ measured by digital lux meter Peak Tech 5025) placed in a vertically oriented dip tube, immersed in the continuously agitated reaction mixture. The photocatalytic reaction was performed up to 120 minutes illumination time. During the reaction, 2 mL samples were collected from the reactor at regular time intervals, when the concentration of compounds was monitored using a UV-Vis spectrophotometer with prior removal of the solid catalyst.

The total solubilised bromide ($Br^-$) was determined potentiometrically using a multimeter (CPC 411, Elmetron, Poland) equipped with a bromide ion-selective electrode (EBr-01, Hydromet, Poland) with the silver chloride electrode (RL-100, Hydromet, Poland) as a reference electrode.

We performed reusability tests of the catalyst for a four cycles of photocatalysis. The degradation BPB efficiency calculation equation is shown in eqn (3).

$$D_{\text{eff}}(\%) = \frac{C_0 - C_t}{C_0} \times 100\% \quad (3)$$

$C_0$ is the initial concentration of BPB, and $C_t$ is the concentration at time $t$ (min).

### 2.5 Kinetic simulations

Competitive kinetics simulations were performed with the Kinetiscope™ stochastic kinetic simulation software[16–18] freely available on the authors' web page: **https://www.hinsberg.net/kinetiscope/**. The rate constants of the radical reactions describing the investigated process, required for the competitive kinetics simulation, were taken from the compilation of the rate constants[19] and shown in Table S2.†

## 3. Results and discussion

### 3.1 Photocatalyst characterisation

$MoS_2$ powders of different morphologies have been obtained using a wide variety of methods such as thermal decomposition of ammonium tetrathiomolybdate or amorphous $MoS_3$,[20] high-temperature reaction of the stoichiometric mixture of molybdenum and sulfur powders under vacuum,[21] gas-phase reactions of $H_2S$ and molybdenum oxides under reducing atmosphere.[22,23] There are also reports on high energy synthetic procedures using laser,[24] electron beam,[25] and gamma radiation[26] leading to molybdenum disulphide as nanotubes, fullerene-like, and other curved nanostructures. The solution-based synthesis procedure developed in this paper is simple and convenient could be an alternative to the methods mentioned above. Furthermore, lithium ions present in the reaction mixture can intercalate and interlayer spacing of $MoS_2$.[27] For this reason, the obtained $MoS_2$ material has semiconductor properties.

SEM micrograph (Fig. 1c and d) reveals that the material has a layered structure. The topography of $MoS_2$ was evaluated by AFM measurements. The AFM image shown in Fig. 1b reveals a layered structure of the material with a thickness range of 100–160 nm.

The obtained $MoS_2$ was analysed using XRD measurements (Fig. 2a). The resulting peaks are characteristic for 2H–$MoS_2$ (JCPDS card no 01-087-2416, $P6_3/mmc$)[28] with lattice parameters $a = 3.17 \pm 0.0035$ Å and $c = 14.17 \pm 0.026$ Å. The unit cell is presented in Fig. 2b. Each layer of $MoS_2$ has a plane of hexagonally arranged molybdenum atoms sandwiched between two planes of hexagonally arranged sulfur atoms, with the covalently bonded S–Mo–S atoms in a trigonal prismatic arrangement form a hexagonal crystal structure. The XRD results represented that the obtained materials have a pure phase. Five diffraction peaks were observed, which can be assigned to the (002), (100), (103), (105), and (110) planes of $MoS_2$, the 2θ values are 13.95; 33.3; 39.8; 48.2; and 59.2, respectively. The peak broadening indicates a sheet-like crystallite morphology with an average size of 50 nm. The XRD spectrum of the $MoS_2$ is comparable to that reported by Quilty *et al.*,[29] and Ortis-Quiles and Cabrera.[30] It confirms that the received material is layered. Layered $MoS_2$ generally displays n-type behaviour. The $d_{002}$ line observed at $2\theta = 13.95$ Å showed a shift towards a lower angle regarding bulk 2H–$MoS_2$. The observed shift may be caused by the lattice expansion compared to that report for 2H–$MoS_2$ ($a = 3.16$ Å, $c = 12.29$ Å). This lattice expansion may be ascribed to the folding and randomness in the stacking of the $MoS_2$ layers.[31]

The optical properties of $MoS_2$ were analysed using the UV-Vis spectra (Fig. 2d). The dye degradation efficiency depends on the energy of the photocatalyst energy gap. When using visible light, a photocatalyst with a lower energy gap energy is preferable. The material exhibited a good optical response to ultraviolet and visible light, which was ascribed to its narrow

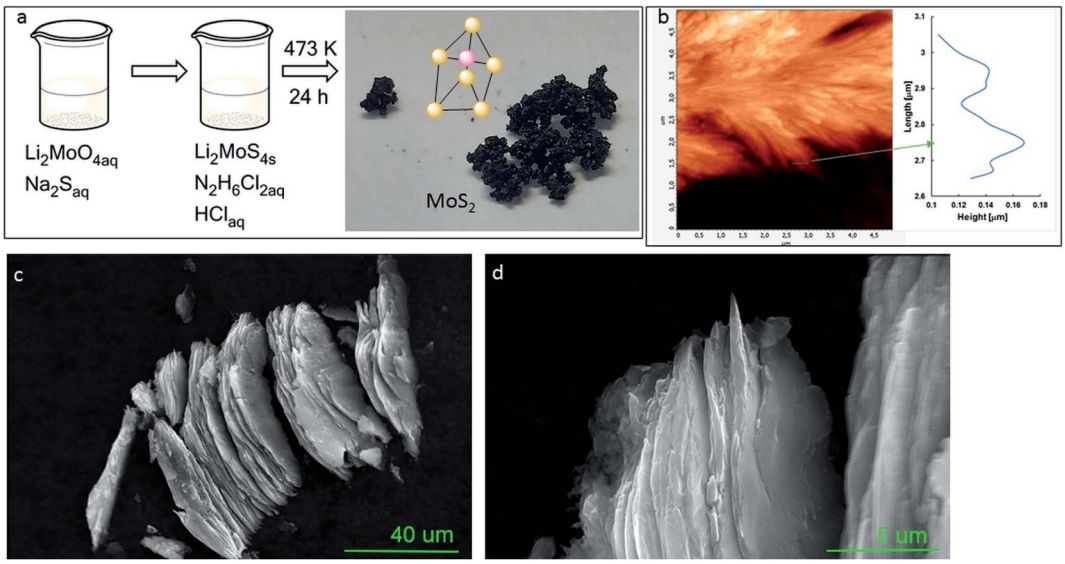


Fig. 1 Schematic description of $MoS_2$ synthesis method (a), AFM image and height profile (b), SEM images of two different points and different magnifications of $MoS_2$ (c and d).

band gap. The band gap width of 2.03 eV was determined from the measurements of the $MoS_2$ absorption spectrum. In addition, absorption peaks at 1.88 eV (659 nm) and 2.08 eV (596 nm) were observed in the spectrum due to the division of the orbit transitions by the spin–orbit coupling.[32,33] The absorption of visible light consequently causes the formation of holes in the valence band by the promotion of electrons to the conduction band.

The recorded Raman spectra contain several bands distinct to the $MoS_2$ material (Fig. 2c). In the spectra, was observed peaks at 375, 404, and 451 $cm^{-1}$, which correlate with the phonon mode of 2H–$MoS_2$. The peak of 2H $MoS_2$ at 378 $cm^{-1}$ corresponds to $E_{2g}{}^1$, due to the opposite vibration of two S atoms regarding the Mo atom, the peak at 404 $cm^{-1}$ is attributed to $A_g{}^1$, associated with the vibration of only S atoms in opposite directions and at 451 $cm^{-1}$ is ascribed to longitudinal acoustic phonon modes.[34] These results demonstrate the 2H–$MoS_2$ structure of the tested material.

Raman spectroscopy may be used for estimating the average number of $MoS_2$ layers. It is known that the distance between the in-plane S atom ($E_{2g}{}^1$) and out-of-plane S atom ($A_{1g}$) vibrational modes corresponds to the crystal thickness. The distance between the $E_{2g}{}^1$ = 378 $cm^{-1}$ and $A_{1g}$ = 404 $cm^{-1}$ vibrational modes was measured, and it was 26 $cm^{-1}$, representing ≤5 layers.[35]

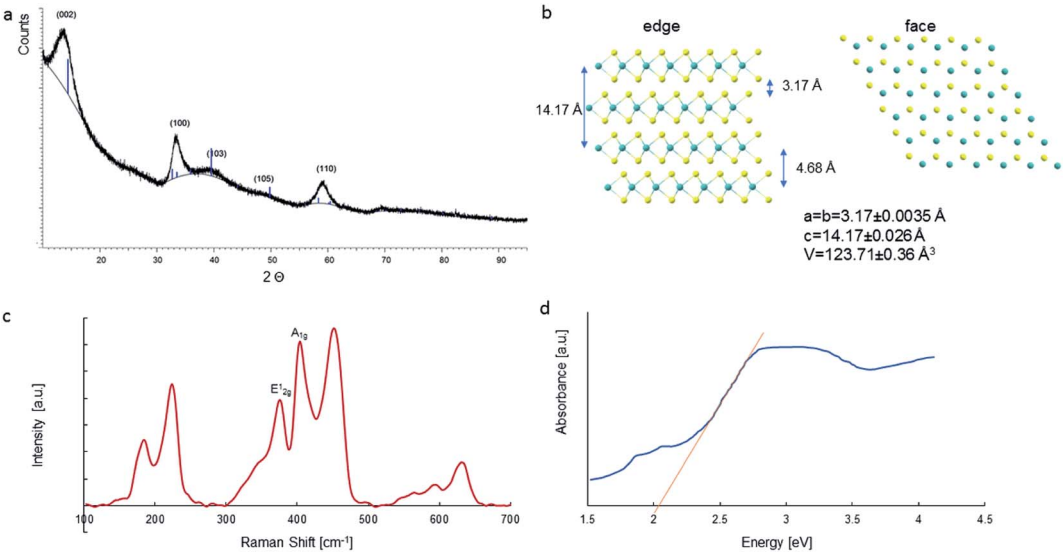


Fig. 2 XRD pattern of the $MoS_2$ sample and (a); Top and side view of $MoS_2$ with the crystal parameters (b); Raman spectra of $MoS_2$ (c); UV-Visible absorption spectra (d).

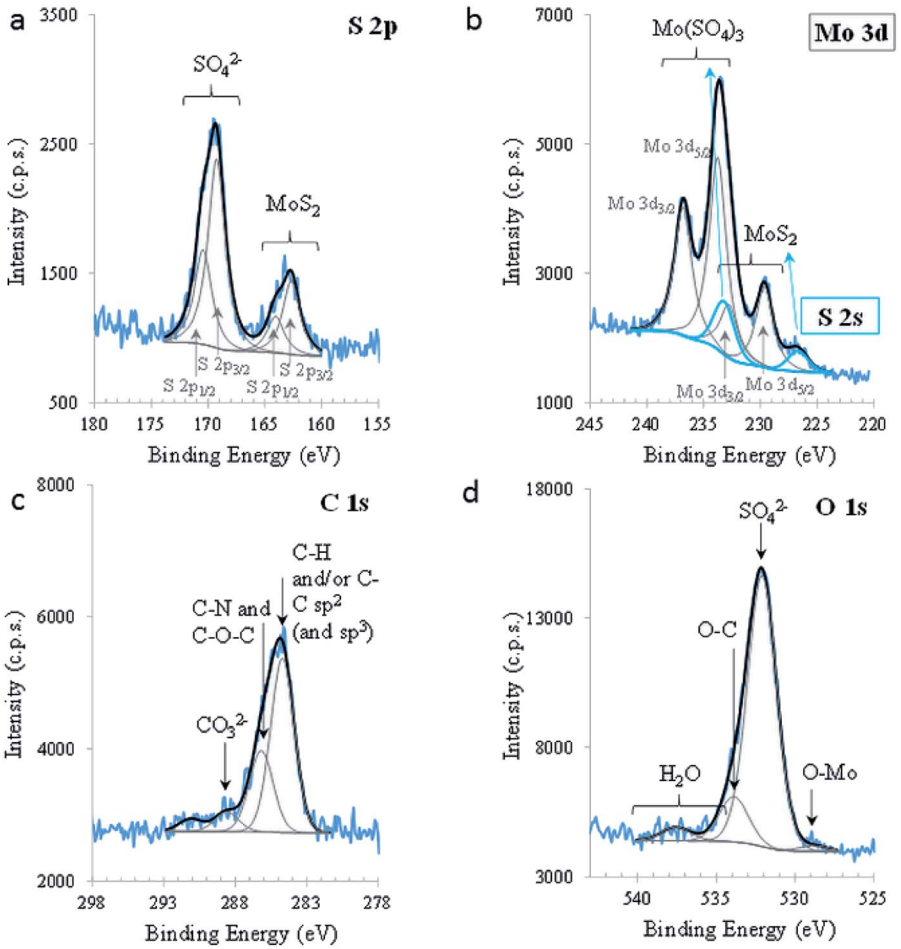


Fig. 3 XPS regions S 2p (a), Mo 3d (and S 2s) (b), C 1s (c), and O 1 s (d).

Absorbance peaks of UV-Vis spectrum at 659 and 596 were utilised as references for determining the particle size and number of $MoS_2$ layers using method previously successfully applied by:[36,37]

$$L = \frac{3.5\dfrac{\mathrm{Abs_B}}{\mathrm{Abs_{350}}} - 0.14}{11.5 - \dfrac{\mathrm{Abs_B}}{\mathrm{Abs_{350}}}},\ (\mu\mathrm{m}) \quad (4)$$

$$N = 2.3 \times 10^{36} \mathrm{e}^{-54888/\lambda_A} \quad (5)$$

where: $Abs_B$ is the absorbance of peak at 596 nm and $Abs_{350}$ is the absorbance of peak at 350 nm in the UV-Vis spectrum.

The calculated particle lateral size ($L$) was 137 nm, while the number of layers was estimated as <5, correlating with Raman characterisation.

To investigate the chemical composition and the nature of the chemical bonds between the elements present in $MoS_2$, XPS was carried out. Fig. 3 shows the relevant XPS regions. S 2p shows clearly the presence of two doublets, with a spin–orbit split (SOS) of 1.3 ± 0.1 eV, with the main components (*i.e.*, S $2p_{3/2}$ components) centred at 162.6 ± 0.1 eV and 169.2 ± 0.1 eV, assigned to S in $MoS_2$ and in $SO_4^{2-}$ groups, respectively. The oxidation of $S_2^-$ in the alkaline medium is predicted by the reaction:

$$SO_{4(aq)}^{2-} + 8e^- + 4H_2O_{(l)} \leftrightarrow S_{(aq)}^{2-} + 8OH_{(aq)}^- \quad (6)$$

Mo 3d is also composed of doublets which, in this case, are overlapping the S 2s region (blue peaks). The peak centred at lower BE (226.7 ± 0.1 eV) is attributed to sulphur (S 2s) in 2D-$MoS_2$. Another peak, centred at 233.2 eV and assigned to sulphur in sulphate groups, was fitted in this region, constraining its area to the same proportion of sulphate/sulphide found in S 2p. Its position was not restricted. Mo 3d is composed of two doublet peaks, with SOS between Mo $3d_{5/2}$ and Mo $3d_{3/2}$ equal to 3.1 (0) eV and a ratio $(3d_{5/2})/(3d_{3/2})$ equal to 1.5; these parameters were imposed for both doublets, leaving Mo $3d_{5/2}$ positions, areas, FWHM and GL free to fit. Mo $3d_{5/2}$ centred at 229.6 ± 0.1 eV and 233.7 ± 0.1 eV are assigned to $Mo^{4+}$ in 2D-$MoS_2$ and to $Mo^{6+}$, respectively. $Mo^{6+}$ is mainly under the form of $Mo(SO_4)_3$ containing also some $MoO_3$, as attested by the $O^{2-}$ peak, centred at 528.8 eV in O 1s, and $Mo(CO_3)_3$, confirmed by the presence of a peak at 288.6 eV in C 1s. The existence of these species is also confirmed by the

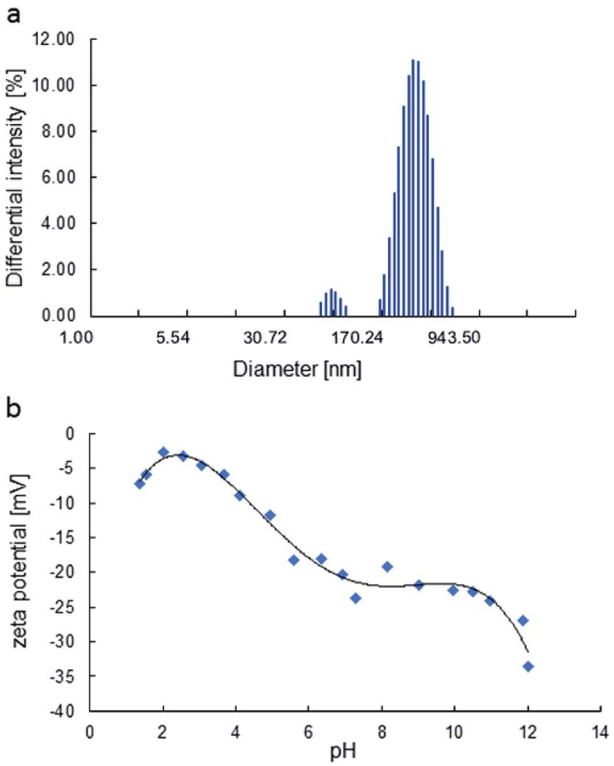


Fig. 4 The particle size distribution of the $H_2O$ dispersion, obtained by DLS (a), zeta potential of $MoS_2$ as a function of pH (b).

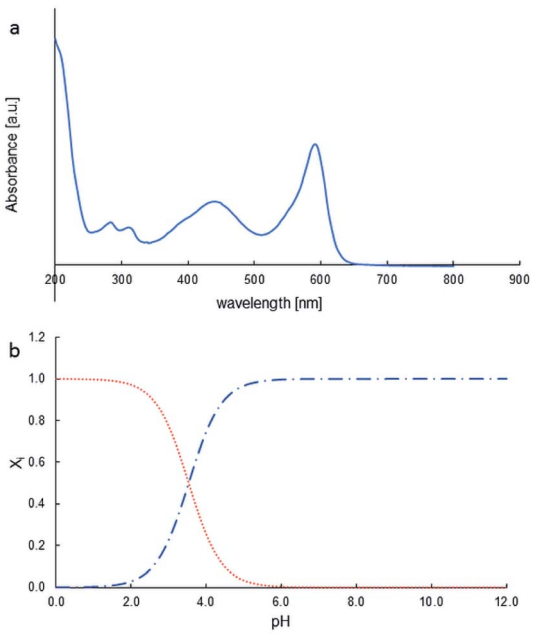


Fig. 5 BPB UV-Vis spectrum (a); distribution of species as pH function, $BPB^-$ (••• red), $BPB^{2-}$ (–•– blue) (b).

quantitative analysis (Table S1†). Oxidation to $Mo^{6+}$ in an alkaline medium is predicted by the reaction:

$$MoO_{4(aq)}^{2-} + 2e^- + 2H_2O_{(l)} \leftrightarrow MoO_{2(s)} + 4OH_{(aq)}^- \quad (7)$$

The valence band (VB) extracted from the XPS spectrum was also analysed. The energy levels are referred to the Fermi level ($E_F$) stated in Fig. S1.† The top of the VB is 1.6 eV, apart from the $E_F$. The fine spectral structure perceived between the top of VB and $E_F$, may be assigned to the density of states. The XPS results confirmed the behaviour of $MoS_2$ semiconductors as n-type.

The particle size of $MoS_2$ in $H_2O$ was also evaluated by DLS (considering their hydrodynamic radius), where the platelet sizes were ranging from 72 to 564 nm (Fig. 4 a). The zeta potential dictates the sign and amount of surface charge in relation to the surrounding conditions. The zeta potentials were negative for all ranges of pH (Fig. 4 b) and decrease with pH. The face/edge ratio (hydrophobic – sulphur surface/metallic – hydrophilic edge) strongly influences the magnitude of the zeta potential being inversely proportional.[38]

The zeta potential of molybdenite particles is due to the generation of electric charges at the edges of the particles, since the faces present only van der Waals forces and no electric charge.[39] The processes on the molybdenite edges can be described:

$$MoS_xO_y + H_2O \leftrightarrow \left[MoS_xO_{\left(y+\frac{n}{2}\right)}\right]^{n-} + 2H^+ \quad (8)$$

$$\left[MoS_xO_{\left(y+\frac{n}{2}\right)}\right]^{n-} + H^+ \leftrightarrow \left[MoS_xO_{\left(y+\frac{n}{2}\right)}\right]^{(n+1)-} \quad (9)$$

These reactions explain the pH decrease of molybdenite powders dispersed in water. The next equation describes the process under alkaline conditions.

$$HMoO_4^- \leftrightarrow H^+ + MoO_4^{2-},\ pK_a = 5.95 \quad (10)$$

It explains the high negative values of zeta potential in high pH conditions.

Wan *et al.*[40] reported that the zeta potential of molybdenite was mainly determined by edges and not faces, especially in the case of fine particles. Compared to the hydrophobic surfaces, the edges of the molybdenite oxidised more easily in the solution.

### 3.2 Evaluation of photocatalytic properties

The photocatalytic properties of $MoS_2$ materials depend on a variety of parameters, such as particle size, number of layers, and the face/edge ratio. The photocatalytic properties of $MoS_2$ were tested in bromophenol blue (BPB) degradation. Fig. 5a presents the BPB absorption spectrum. Diagnostic was the peak at 590 nm for dye decay monitoring.

The photocatalytic activity tests of the synthesised $MoS_2$ were evaluated by carrying out the degradation of bromophenol blue in weak acidic aqueous solution (pH 5.2). Under such conditions, BPB is present in solution only in the fully dissociated form; the respective first and second acid dissociation constants, pKa, are 3.00 and 4.6 (Fig. 5b, and 6). The simulated (using $pK_a$ of compound and Curtipot software[41]) molar fraction

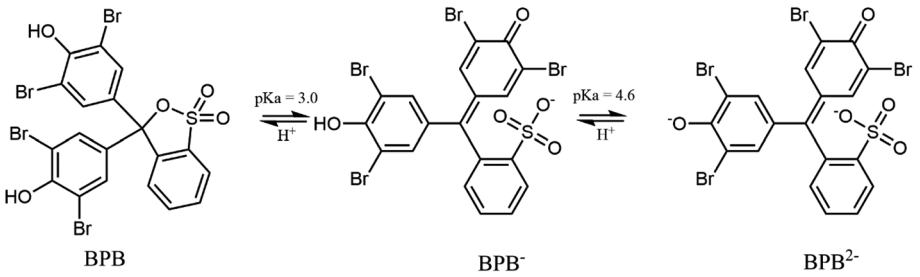


Fig. 6 Dissociation equilibrium of the pH indicator BPB.

of ionic forms at pH 5.2 is $BPB^{2-}$ 0.979, $BPB^{-}$ 0.021, BPB 0.00 (Fig. 4b).

The progress of the photodegradation reaction was monitored by recording changes in the concentration of the BPB solution at regular intervals. Fig. 7 represents the results for the photocatalytic degradation of the BPB dye using $MoS_2$ as the photocatalyst.

Almost over the entire time region, the substrate decays obey the pseudo-first-order kinetics eqn (11):

$$\ln\frac{C_t}{C_0} = -k_{app}t \quad (11)$$

where $k_{app}$ is the apparent rate constant; $C_0$ and $C_t$ are the initial concentration and concentration at time $t$.

The depletion of BPB concentration occurs mainly due to the photocatalytic properties of the synthesised materials and not because of the photolysis of the dye (Fig. 7b). For $MoS_2$, the degradation efficiency of the BPB dye was very high and was found to be 100% for a time of 40 min.

A plot of $\ln(C/C_0)$ *versus* time yields a straight line where $k_{app}$ is the slope (see Fig. 7c). Photocatalytic activities of the catalysts were estimated by monitoring the decomposition of dye in the catalyst suspension upon illumination. The half-lives of decay ($t_{1/2}$) were 6.7 min and the apparent rate constants ($k_{app}$) calculated from the plots were $103.7 \times 10^{-3}$ $min^{-1}$.

The efficacy of catalysis depends on the catalyst–substrate interactions. The negative zeta potential of our molybdenite particles (*ca.* −14.4 mV) suggests anions in the Stern layer. Thus, in particular, in reaction conditions, the BPB-dianion ($BPB^{2-}$) can be present in the vicinity of the $MoS_2$ surface, probably near its Mo-built metallic edge. It allows the surface-substrate electron transfer, and reductive debromination of $BPB^{2-}$ and relatively high $k_{app}$, indicating the catalytic activity of $MoS_2$.

Observed debromination can indicate the reducing pathway of BPB degradation. The release of bromide in time depicts Fig. 7d. Electron transfer-induced dehalogenation of halogenated organic compounds is a common mechanism in their redox chemistry.[42] There are cases where electron transfer to a neutral precursor leaves the resulting radical ion in an electronic ground state that is dissociative. The process is called dissociative attachment.[43] Following an electron transfer event, which is rapid on the timescale of nuclear motion, the ion relaxes along the dissociation coordinate, breaking one or more

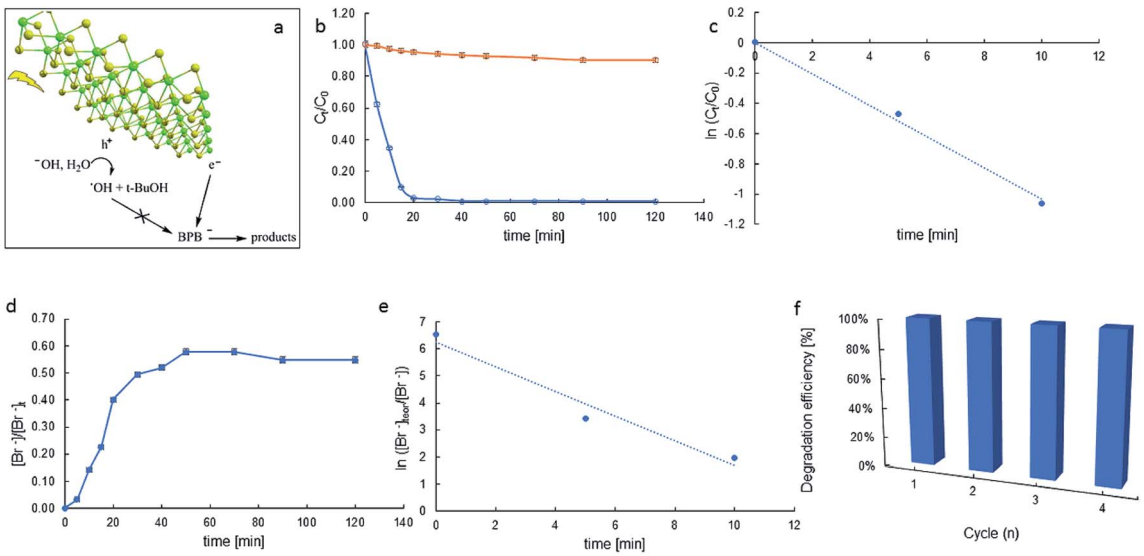


Fig. 7 Schematic description of BPB photocatalytic degradation (a), BPB decay in time in the photocatalytic process (blue), and photolysis (orange) (b); $k_{app}$ determination (c); bromide production in time (d); apparent rate constant ($k_{app}$) for bromide generation determination (e); reusability of catalyst (f).

bonds. For aromatic halides, the reductive cleavage is believed to occur in a two-step mechanism ($RX + e^- \rightarrow RX^{\cdot} \rightarrow R^{\cdot} + X^-$) with the transient formation of a radical anion ($RX^{\cdot -}$). In particular, the accelerated degradation of BPB indicates the reductive debromination to be very efficient ($k_{app} = 457.4 \times 10^{-3}$ min$^{-1}$, Fig. 7e).

The observed dye degradation occurs mainly as a result of reactions with the present on the catalyst surface $e^-$ and $h^+$, since hydroxyl radicals ($^{\cdot}OH$) in the bulk of the solution are scavenged by *t*-BuOH, while saturation with argon eliminates oxygen in the solution and the potential formation of superoxide radicals ($O^{2\cdot -}$). This confirms that electron mobility plays a major role in the photocatalytic degradation of BPB. It is assumed that the radicals formed as by-products of *t*-BuOH reaction with OH and H radicals are neutral.[44]

The $MoS_2$ layer structure is favourable for the separation of charge carriers. The presence of a positive and negative charge density on the Mo and S terminated surfaces, respectively, produces a polarisation effect across these nanosheets, which causes an effective separation of the electron–hole pair and facilitates the movements of a photogenerated electron across the nanosheets. In photocatalytic oxidation processes, photogenerated holes in the valence band play a significant role. The valence band edge potential for $MoS_2$ was estimated to be 1.6 V, which is not oxidative enough to generate hydroxyl radicals ($^{\cdot}OH$). In addition, the reaction conditions were chosen so as (presence of *t*-BuOH, argon purging) to eliminate the oxidising agents such as hydroxyl radicals and/or superoxide radicals. The oxidation potential of BPB is +0.78 V,[45] so BPB could be oxidised by holes. This process may be limited by the repulsion between the BPB and the catalyst surface.

However, recombination of the electron–hole pair is prevented by the presence of BPB molecules. These molecules can interact strongly with the generated electrons. Since the surface of the catalyst is negatively charged and the BPB molecule is negatively charged, strong repulsive forces occur there. Simultaneously, a reaction of BPB with a photocatalytically generated electron was observed. It suggests an interaction between the surface of the BPB molecule and the catalyst by relatively weak London forces.[46]

Based on the obtained kinetic results and simulation of the kinetics of the BPB degradation reaction, a suitable reaction path for the degradation of BPB has been proposed, as shown in Scheme 1:

$$MoS_2 + h\nu \rightarrow MoS_2(h^+ + e^-)$$
$$MoS_2(h^+) + H_2O \rightarrow MoS_2 + {}^{\cdot}OH + H^+$$
$$MoS_2(h^+) + OH^- \rightarrow MoS_2 + {}^{\cdot}OH$$
$$H^+ + e^- \rightarrow H^{\cdot}$$
$$2H^{\cdot} \rightarrow H_2$$
$$BPB^{2-} + e^- \rightarrow BPB^{2-\cdot} + Br^-$$
$$BPB^{2-} + H^{\cdot} \rightarrow [BPBH]^{2-\cdot} + Br^-$$
$$(CH_3)_3OH + {}^{\cdot}OH \rightarrow {}^{\cdot}CH_2C(CH_3)_2OH + H_2O$$
$$(CH_3)_3OH + {}^{\cdot}H \rightarrow {}^{\cdot}CH_2C(CH_3)_2OH + H_2$$

Scheme 1 Proposed reaction path for the BPB degradation.

Since the Kinetiscope™ software does not provide automatic fitting ability, we worked through trial and error. The best match of BPB decay, presented in Fig. S2,† was obtained immediately for the rate constants ($k_{(BPB+e)}$ and $k_{(BPB+H)}$) equal to $1.1 \times 10^{10}$ and $2 \times 10^9$ mol dm$^{-3}$, respectively, while the product of luminous flux and quantum yield *i.e.* 'hole and electron production yield' was set equal to concentration of the catalyst in the suspension. The best match of $Br^-$ formation yield was obtained when the rate of electron with secondary, partially dehalogenated products was set proportional to the number of remaining bromine atoms in the molecule (*i.e.* 3/4, 1/2 and 1/4 of $k_{(BPB+e)}$).

The reusability of the catalysts is an important aspect for practical applications, and was evaluated for four successive runs. Four runs of BPB degradation reactions were investigated. As shown in Fig. 7f, the degradation rates after 60 min reached 99.3, 97.5, 93.1, and 89.9%, respectively. These results show layered $MoS_2$ has high photocatalytic efficiency and good recycling performance.

Several articles have been written regarding the degradation of dyes. The BPB is a convenient model compound due to its high water solubility and the possibility of degradation in both oxidation and reduction processes. However, most of the works on BPB degradation describe oxidative processes.

Shah T. *et al.*[47] in their study examined the photodegradation of BPB dye in an aqueous medium by graphene nanoplates-supported titanium dioxide ($TiO_2$/GNP). The photodegradation study was performed as a function of time, and it was found that the photodegradation of dye in an aqueous medium increased as the time duration of UV irradiation increased. It was found that about 86% of dye was degraded within 8 h. The degradation of bromophenol blue is pH dependent and the rate of photodegradation increased with increasing solution pH, which could be due to the formation of more hydroxyl radicals at higher pH. The degradation of dye at pH 2, 4, 6, and 8 was about 70, 79, 90, and 95%, respectively. There were no data on the degradation reaction rate constants in the article.

Shah U. *et al.* in their recent study[48] researched BPB photocatalytic degradation on two catalysts: zinc sulphide (ZnS) and tin-doped zinc sulphide (Sn–ZnS). About 86% and 96% dye degradation was observed in 300 min. The rate of dye degradation was found to increase with the increase in temperature (up to 70 °C) and pH (9.5). The recyclability study showed that both pure ZnS and Sn–ZnS NPs could be reused for the degradation of BPB. The mechanism proposed by Shah *et al.* describes the degradation of BPB under oxidative conditions. The photocatalytic degradation process was carried out in the temperature range from 40 to 70 °C. The obtained pseudo-first-order rate constants were in the range $4.7 \times 10^{-3}$–$11.4 \times 10^{-3}$ min$^{-1}$ and $5 \times 10^{-3}$–$14.5 \times 10^{-3}$ for ZnS and Sn–ZnS, respectively.

Razavi *et al.*[49] investigated the photocatalytic ability of $Ti_x$-$Ni_yLa_mO_z$ to degrade bromophenol blue in their recent work. The results show this catalyst can remove BPB from the aqueous solution. The authors tested several parameters influencing the rate of degradation. The resulting pseudo-first rate reaction

constants were in the range of $0.7 \times 10^{-3}$–$7 \times 10^{-3}$ $min^{-1}$. The degradation process was carried out under oxidative conditions.

The photocatalytic activities of the fluorinated $TiO_2$ composites with carbon nanotubes (CNTs–$TiO_2$–F) were evaluated with BPB in Dlamini *et al.* article.[50] Rapid photocatalytic degradation of BPB by CNTs–$TiO_2$–F was observed with a percentage removal of 98% of BPB at 20 min of illumination. The as-prepared $TiO_2$ showed the least photoactivity of all four catalysts, degrading up to 85% of BPB at 140 min. CNTs–$TiO_2$ and $TiO_2$–F, degraded BPB up to 94% in140 min irradiation time. The reaction kinetics show the reactions followed a pseudo-first order, increasing from $17.8 \times 10^{-3}$ $min^{-1}$ ($TiO_2$) to $67.3 \times 10^{-3}$ $min^{-1}$ (CNTs–$TiO_2$–F). The photodegradation mechanism was oxidative.

The degradation processes shown in papers[47–50] rely on photo-oxidation undergoing upon the UV-irradiation of highly-engineered nanomaterials. While our approach, based on photo-reduction, offers similar effectiveness of defluorination on material absorbing both UV and visible light. We believe that our methodology of layered $MoS_2$-synthesis sets up a space for further modification and improvement of in-use performance.

# 4 Conclusions

We have shown a feasible method for synthesising layered $MoS_2$. The proposed method resulted in the improvement of the catalytic properties of $MoS_2$ such as light harvesting, avoiding fast charge recombination, and creating numerous appropriate sites for electron transfer. The morphology, optical properties, surface properties and photocatalytic features of $MoS_2$ were investigated.

The photocatalytic efficiency of the material was evaluated for the degradation of bromophenol blue dye. The degradations were conducted under reductive conditions (argon purging, hydroxyl radical scavenging). To propose the sequence of reactions taking place during the degradation process, simulations of the reaction kinetics were performed. Our work shows that $MoS_2$ is a highly efficient photocatalyst for the reduction processes. After four cycles, the removal effectiveness was still as high as 89.9%

From the presented studies, it can be concluded that $MoS_2$ may serve as an effective photocatalyst for environmental remediation. These studies can help in the development of cheap and effective water and wastewater treatment using advanced reduction processes (especially for the degradation of polyhalogenated arenes).

# Author contributions

Joanna Kisała: conception and design of study, analysis and interpretation of data, writing original draft. Ana M. Ferraria: data acquisition, analysis and interpretation of data. Nataliya Mitina: synthesis of material. Bogumił Cieniek: XRD data acquisition, analysis and interpretation of data. Piotr Krzemiński: SEM, AFM data acquisition, analysis and interpretation of data. Dariusz Pogocki: kinetic simulations data acquisition, analysis and interpretation of data, Roman Nebesnyi: analysis and interpretation of data, Oleksandr Zaichenko: analysis and interpretation of data, Yaroslav Bobitski: analysis and interpretation of data, group supervising.

# Conflicts of interest

There are no conflicts to declare.

# Acknowledgements

A. M. Ferraria thanks FCT-Portuguese Foundation for Science and Technology within the scope of research units grants to iBB (UIDB/04565/2020 and UIDP/04565/2020) and i4HB (LA/P/0140/2020) and Instituto Superior Técnico for the Scientific Employment contract IST-ID/131/2018. The authors are grateful to Dr Renata Wojnarowska-Nowak for carrying out measurements of the Raman spectra.

# References

1 M. Lučić, N. Milosavljević, M. Radetić, Z. Šaponjić, M. Radoičić and M. K. Krušić, The potential application of $TiO_2$/hydrogel nanocomposite for removal of various textile azo dyes, *Sep. Purif. Technol.*, 2014, **122**, 206–216.
2 R. Azmat, Z. Khalid, M. Haroon and K. Perveen, Spectral analysis of catalytic oxidation and degradation of bromophenol blue at low pH with potassium dichromate, *Adv. Nat. Sci.*, 2013, **6**, 38–43.
3 N. Li, J. Zhang, C. Wang and H. Sun, Enhanced photocatalytic degradation of Tetrabromobisphenol A by tourmaline-$TiO_2$ composite catalyst, *J. Mater. Sci.*, 2017, **52**, 6937–6949.
4 R. Weng, F. Tian, Z. Yu, J. Ma, Y. Lu and B. Xi, Efficient mineralization of TBBPA *via* an integrated photocatalytic reduction/oxidation process mediated by $MoS_2/SnIn_4S_8$ photocatalyst, *Chemosphere*, 2021, **285**, 131542.
5 J. B. Kisała, G. Hörner, A. Barylyak, D. Pogocki and Y. Bobitski, Photocatalytic Degradation of 4,4′-Isopropylidenebis(2,6-dibromophenol) on Sulfur-Doped Nano $TiO_2$, *Materials*, 2022, **15**, 361.
6 H. J. Conley, B. Wang, J. I. Ziegler, R. F. Haglund Jr, S. T. Pantelides and K. I. Bolotin, Bandgap Engineering of Strained Monolayer and Bilayer $MoS_2$, *Nano Lett.*, 2013, **13**, 3626–3630.
7 C. Feng, J. Ma, H. Li, R. Zeng, Z. Guo and H. Liu, Synthesis of molybdenum disulfide ($MoS_2$) for lithium ion battery applications, *Mater. Res. Bull.*, 2009, **44**, 1811–1815.
8 F. R. Wang, Y.-Y. Su, J.-K. Liu and Y. Wu, Enhanced photoelectric properties by the coordinating role of doping and modification, *Phys. Chem. Chem. Phys.*, 2016, **18**, 4850–4859.
9 H. Hwang, H. Kim and J. Cho, $MoS_2$ Nanoplates Consisting of Disordered Graphene-like Layers for High Rate Lithium Battery Anode Materials, *Nano Lett.*, 2011, **11**, 4826–4830.
10 X. Man, L. Yu, J. Sun and S. Li, The synthesis and the photocatalytic degradation property of the nano-$MoS_2$, *Funct. Mater. Lett.*, 2016, **9**, 1650065.

11 B. P. Vellanki and B. Batchelor, Perchlorate reduction by the sulfite/ultraviolet light advanced reduction process, *J. Hazard. Mater.*, 2013, **262**, 348–356.
12 Q. Xiao, S. Yu, L. Li, T. Wang, X. Liao and Y. Ye, An overview of advanced reduction processes for bromate removal from drinking water: Reducing agents, activation methods, applications and mechanisms, *J. Hazard. Mater.*, 2017, **324**, 230–240.
13 P. Scherrer, Bestimmung der Grosse und der Inneren Struktur von Kolloidteilchen Mittels Rontgenstrahlen, *Nachrichten von Der Gesellschaft Der Wissenschaften. Gottingen. Math. Klasse*, 1918, **2**, 98–100.
14 J. I. Langford and A. J. C. Wilson, Scherrer after sixty years: A survey and some new results in the determination of crystallite size, *J. Appl. Crystallogr.*, 1978, **11**, 102–113.
15 Z. Hamden, S. Bouattour, A. M. Ferraria, D. P. Ferreira, L. F. Vieira Ferreira, A. M. Botelho do Rego and S. Boufi, In-situ generation of $TiO_2$ nanoparticles using chitosan as a template and its photocatalytic activity, *J. Photochem. Photobiol., A*, 2016, **321**, 211–222.
16 D. L. Bunker, B. Garrett, T. Kleindienst and G. S. Long, Discrete simulation methods in combustion kinetics, *Combust. Flame*, 1974, **23**, 373–379.
17 D. T. Gillespie, General method for numerically simulating stochastic time evolution of coupled chemical-reactions, *J. Comput. Phys.*, 1976, **22**, 403–434.
18 W. Hinsberg and F. A. Houle, *KinetiscopeTM a Stochastic Kinetics Simulator*, Columbia Hill Technical Consulting, Fremont, California, 2017. **https://hinsberg.net/kinetiscope/index.html**.
19 G. V. Buxton, C. L. Greenstock, W. P. Helman and A. B. Ross, Critical-Review of Rate Constants for Reactions of Hydrated Electrons, Hydrogen-Atoms and Hydroxyl Radicals ($^{\cdot}OH/^{\cdot}O^{-}$) in Aqueous-Solution, *J. Phys. Chem. Ref. Data*, 1988, **17**, 513–886.
20 M. Nath, A. Govindaraj and C. N. R. Rao, Simple synthesis of $MoS_2$ and $WS_2$ nanotubes, *Adv. Mater.*, 2001, **13**, 283–286.
21 R. N. Viswanath and S. Ramasamy, Preparation and isochronal sintering behavior of molybdenum disulfide compound, *J. Mater. Sci.*, 1990, **25**, 5029–5035.
22 Y. Feldman, G. L. Frey, M. Homyonfer, V. Lyakhovitskaya, L. Margulis, H. Cohen, G. Hodges, J. L. Hutchinson and R. Tenne, Bulk synthesis of inorganic fullerene-like $MS_2$ (M = Mo, W) from the respective trioxides and the reaction mechanism, *J. Am. Chem. Soc.*, 1996, **118**, 5362–5367.
23 Y. Feldman, E. Wasserman, D. J. Srolovitz and R. Tenne, High rate, gas-phase growth of $MoS_2$ nested inorganic fullerenes and nanotubes, *Science*, 1995, **267**, 222–225.
24 P. A. Parilla, A. C. Dillon, K. M. Jones, G. Riker, D. L. Schulz, D. S. Ginley and M. J. Heben, The first true inorganic fullerenes?, *Nature*, 1999, **397**, 114.
25 M. J. Yacamán, H. López, P. Santiago, D. H. Galván, I. L. Garzón and A. Reyes, Studies of $MoS_2$ structures produced by electron irradiation, *Appl. Phys. Lett.*, 1996, **69**, 1065–1067.
26 G. Chu, G. Bian, Y. Fu and Z. Zhang, Preparation and structural characterization of nano-sized amorphous powders of $MoS_2$ by $\gamma$-irradiation method, *Mater. Lett.*, 2000, **43**, 81–86.
27 X. Fan, P. Xu, D. Zhou, Y. Sun, Y. C. Li, M. A. T. Nguyen, M. Terrones and T. E. Mallouk, Fast and efficient preparation of exfoliated 2H $MoS_2$ nanosheets by sonication assisted lithium intercalation and infrared laser-induced 1T to 2H phase reversion, *Nano Lett.*, 2015, **15**, 5956–5960.
28 *PDF-2 2021 (Database)*, ed. S. Kabekkodu, International Centre for Diffraction Data, Newtown Square (PA)(2021).
29 C. D. Quilty, L. M. Housel, D. C. Bock, M. R. Dunkin, L. Wang, D. M. Lutz, A. Abraham, A. M. Bruck, E. S. Takeuchi, K. J. Takeuchi and A. C. Marschilok, *Ex Situ* and Operando XRD and XAS Analysis of $MoS_2$: A lithiation study of bulk and Nanosheet Materials, *ACS Appl. Energy Mater.*, 2019, **2**, 7635–7646.
30 E. O. Ortiz-Quiles and C. R. Cabrera Jr, Exfoliated molybdenum disulphide for dye sensitized solar cells, *FlatChem*, 2017, **2**, 1–7.
31 Z. Wu, D. Wang and A. Sun, Surfactant-assisted fabrication of $MoS_2$ nanospheres, *J. Mater. Sci.*, 2010, **45**, 182–187.
32 A. M. Stacy and D. T. Hodul, Raman spectra of IV-V and VIB transition metal disulfides using laser energies near the absorption edges, *J. Phys. Chem. Solids*, 1985, **46**, 405–409.
33 B. C. Windom, W. G. Sawyer and D. W. Hahn, A Raman Spectroscopic Study of $MoS_2$ and $MoO_3$: Applications to Trbological Systems, *Tribol. Lett.*, 2011, **42**, 301–310.
34 J.-H. Fan, P. Gao, A.-M. Zhang, B.-R. Zhu, H.-L. Zeng, X.-D. Cui, R. He and Q.-M. Zhang, Resonance Raman scattering in bulk 2H-$MX_2$ (M = Mo, W; X = S, Se) and monolayer $MoS_2$, *J. Appl. Phys.*, 2014, **115**, 053527.
35 L. Liang and V. Meunier, First-principles Raman spectra of $MoS_2$, $WS_2$ and their heterostructures, *Nanoscale*, 2014, **29**, 243–255.
36 C. Backes, R. J. Smith, N. McEvoy, N. C. Berner, D. McCloskey, H. C. Nerl, A. O'Neill, P. J. King, T. Higgins, D. Hanlon, N. Scheuschner, J. Maultzsch, L. Houben, G. S. Duesberg, J. F. Donegan, V. Nicolosi and J. N. Coleman, Edge and confinement effects allow *in situ* measurement of size and thickness of liquid-exfoliated nanosheets, *Nat. Commun.*, 2013, **5**, 4576.
37 C. L. C. Rodriguez, P. A. R. Munoz, K. Z. Donato, L. Seixas, R. K. Donato and G. J. M. Fechine, Understanding the unorthodox stabilization of liquid phase exfoliated molybdenum disulfide ($MoS_2$) in water medium, *Phys. Chem. Chem. Phys.*, 2020, **22**, 1457–1465.
38 J. O. Tabares, I. M. Ortega, J. L. Reyes Bahena, A. A. Sanchez Lopez, D. Valdez Perez and A. Lopez-Valdivieso, Surface Properties and Floatability of Molybdenite, *Proceedings of the 2006 China-Mexico Workshop on Minerals Particle Technol.*, San Luis Potosi, Mexico, 2006, pp. 115–124.
39 D. W. Fuerstenau and S. Chander, On the natural floatability of molybdenite, *Transactions SME*, 1972, **255**, 62–69.
40 H. Wan, W. Yang, W. Cao, T. He, Y. Liu, J. Yang, L. Guo and Y. Peng, The Interaction between $Ca^{2+}$ and Molybdenite Edges and Its Effect on Molybdenum Flotation, *Minerals*, 2017, **7**, 141.

41 I. G. R. Gutz, *pH Calculation and Acid-Base Titration Curves – Freeware for Data Analysis and Simulation, (n.d.)*, **https://www.iq.usp.br/gutz/Curtipot_.html**, (accessed April 6, 2020).
42 A. A. Isse, P. R. Mussini and A. Gennaro, New Insights into Electrocatalysis and Dissociative Electron Transfer Mechanisms: The Case of Aromatic Bromides, *J. Phys. Chem. C*, 2009, **113**, 14983–14992.
43 P. Andrieux, C. Blocman, J. M. Dumas-Bouchiat and J. M. Saveant, Heterogeneous and homogeneous electron transfers to aromatic halides. An electrochemical redox catalysis study in the halobenzene and halopyridine series, *J. Am. Chem. Soc.*, 1979, **101**, 3431–3441.
44 M. Sánchez-Polo, J. López-Peñalver, G. Prados-Joya, M. A. Ferro-García and J. Rivera-Utrilla, Gamma irradiation of pharmaceutical compounds, nitroimidazoles, as new alternative for water treatment, *Water Res.*, 2009, **43**, 4028–4036.
45 G.-J. Yang, Xi-L. Qu, Ai-P. Zhu, C.-Y. Wang, Qi-S. Qu and X.-Ya Hu, Characterization, growth mechanism and application of network poly(bromophenol blue), *J. Electroanal. Chem.*, 2007, **604**, 48–56.
46 J. P. Wagner and P. R. Schreiner, London dispersion in molecular chemistry—reconsidering steric effects, *Angew. Chem., Int. Ed.*, 2015, **54**, 12274–12296.
47 T. Shah, T. Gul and K. Saeed, Photodegradation of bromophenol blue in aqueous medium using graphene nanoplates-supported $TiO_2$, *Appl. Water Sci.*, 2019, **9**, 105.
48 U. Shah, F. Akbar Jan, R. Ullah, W. Salman and N. Ullah, Tin decorated Zinc Sulphide Nanoparticles for Photocatalytic Degradation of Bromophenol Blue Dye and Their Therapeutic Applications: A Kinetic and Thermodynamic Approach, *ECS J. Solid State Sci. Technol.*, 2022, **11**, 033011.
49 M. R. Razavi, Y. Absalan, M. Gholizadeh, S. Strashnov and O. Kovalchukova, Removal of bromophenol blue by $Ti_xNi_yLa_mO_z$ photocatalyst under various conditions, *Environ. Technol. Innovation*, 2022, **26**, 102385.
50 L. N. Dlamini, R. W. Krause, G. U. Kulkarni and S. H. Durbach, Photodegradation of bromophenol blue with fluorinated $TiO_2$ composite, *Appl. Water Sci.*, 2011, **1**, 19–24.